

## GSA Data Repository 2018129

### Fracture density and grain size controls on the relief structure of bedrock landscapes

Roman A. DiBiase<sup>1</sup>, Matthew W. Rossi<sup>2</sup>, Alexander B. Neely<sup>1</sup>

<sup>1</sup>Department of Geosciences, Pennsylvania State University, University Park, PA 16802, USA

<sup>2</sup>Earth Lab, University of Colorado, Boulder, CO 80309, USA

\*To whom correspondence may be addressed: Roman A. DiBiase, rad22@psu.edu

### Contents

**Supplementary methods:** Additional methodological details.

**Supplementary table:**

**Table DR1.** Parameters used for stochastic-threshold incision model.

**Table DR2.** Cosmogenic nuclide erosion rate data and sources used in Fig. 3c.

**Supplementary figures:**

**Figure DR1.** Overview maps of Eastern San Gabriel Mountains (ESGM) and Northern San Jacinto Mountains (NSJM) showing geology, mean annual temperature, and mean annual precipitation.

**Figure DR2.** Comparison of runoff records for Cucamonga Creek (ESGM) and Snow Creek (NSJM) during 16 year period of overlapping records beginning water year 1960.

**Figure DR3.** Daily runoff records for Cucamonga Creek and Snow Creek for the overlapping period water year 1960-1975.

**Figure DR4.** Plan view and slope-corrected kernel density plots of hillslope angle for the Eastern San Gabriel Mountains (ESGM) and Northern San Jacinto Mountains (NSJM).

**Figure DR5.** Comparison of photographs and lidar point cloud data of bedrock cliffs shown in Fig 2a and Fig 2b.

**Figure DR6.** Orthophotos of reaches used for grain size and width analysis.

**Figure DR7.** Chi-elevation plots of mainstem channels in the ESGM (blue) and NSJM (red), highlighting range of channel steepness index for each landscape.

**Figure DR8.** Colluvial channel slope analysis for the ESGM and NSJM.

**Figure DR9.** Oblique air photographs of ESGM cliffs analyzed in Fig. 2c.

**Figure DR10.** Oblique air photographs of NSJM cliffs analyzed in Fig. 2c.

**Supplementary dataset S1:** "2018129 Cliff Outlines.kml" contains georeferenced outlines of all bedrock cliffs used for analysis of Figure 2c.

### References Cited

## Supplementary Methods

**Kernel density plots of hillslope angle.** We used 1 m bare-earth, lidar-derived digital elevation models of the Northern San Jacinto Mountains (NSJM) and the Eastern San Gabriel Mountains (ESGM) to calculate local slope at each grid cell based on the 3x3 neighborhood algorithm in ArcGIS. After masking out channel fill and river terraces, we constructed kernel density plots of hillslope angle using a kernel density estimation with a slope bandwidth of  $0.3^\circ$ . As a proxy for the fraction of bedrock exposed on steep hillslopes, we calculated the fraction of slopes steeper than  $45^\circ$  for each landscape, and divided by a correction factor of 1.22 based on calibrations to photographic mapping of bedrock exposure throughout the San Gabriel Mountains (see DiBiase et al., 2012 for methodology and calibration). At steep slopes, plan view calculations substantially under-estimate the surface area represented by each pixel. To account for this plan view distortion in the kernel density plots, we multiplied the projected area by  $1/\cos\theta$ . Numbers reported in the main text are corrected for this slope-effect. Although modal slopes remain similar, accounting for plan view distortion increases the mean slope to  $42^\circ$  in the ESGM and  $47^\circ$  in the NSJM (compared to  $39^\circ$  and  $42^\circ$ , respectively; Fig. DR4).

**Bedrock cliff morphology.** In order to compare the morphology of bedrock hillslopes from each landscape, we identified the 20 largest and steepest cliffs in both the ESGM and the NSJM, and isolated bare-earth point clouds for each cliff face (Fig. DR5). For computational efficiency, we sub-sampled point clouds to a minimum point spacing of 1 m. For each cliff, we calculated the relief,  $\Delta z_{i,j}$ , and slope,  $\theta_{i,j}$ , between all possible pairs of points  $(x_i, y_i, z_i), (x_j, y_j, z_j)$  within the point cloud as:

$$\Delta z_{i,j} = |z_i - z_j| \quad (1)$$

$$\theta_{i,j} = \tan^{-1} \left( \frac{|z_i - z_j|}{\sqrt{(x_i - x_j)^2 + (y_i - y_j)^2}} \right). \quad (2)$$

We extracted maximum relief for results binned by slope ( $1^\circ$  slope bins) to define an envelope of maximum relief,  $\Delta z_{max}$ , as a function of slope. The data shown in Fig. 2c are cut off at low slopes where the relief-slope curve reaches an inflection point set by the height of the cliff face. This approach is similar in principle to the concept of a limit of topographic development used by Schmidt and Montgomery (1995), and provides a measure of the scale-dependent morphology of individual cliffs. By selecting the largest and steepest cliff faces, we aimed to identify areas in the landscape that are most likely to be at the threshold of stability, an assumption that is supported by the similarity of relief envelopes for cliffs within each landscape (Fig. 2c).

To quantify differences in the apparent rock strength of bedrock slopes between the two datasets, we used a Culmann limit-equilibrium prediction of the relationship between slope and relief, based on a Coulomb failure model (Schmidt and Montgomery, 1995):

$$\Delta z_{max} = \frac{4c}{\rho g} \frac{\sin\theta \cos\varphi}{[1 - \cos(\theta - \varphi)]}, \quad (3)$$

where  $\rho$  is bulk density,  $g$  is gravitational acceleration,  $c$  is effective cohesion, and  $\varphi$  is the angle of internal friction of the cliff material. We used a bulk density of  $2650 \text{ kg/m}^3$  for granite and assumed  $\varphi = 35^\circ$ , such that differences in the relief-slope relationship are assumed to be due to

differences in effective cohesion only. We plotted 50 kPa contours of effective cohesion for comparison with lidar-derived relief-slope curves (Fig. 2c). Although Equation (3) is a simplified treatment of the mechanics of bedrock failure in the ESGM and NSJM, the first order behavior encapsulated by the inverse relationship between slope and relief should be characteristic of a wide range of slope-stability models.

We ascribe the contrast in effective cohesion between the ESGM and NSJM primarily to qualitative differences in fracture density between the two landscapes (Fig. 2, Fig. DR9, Fig. DR10). We see no dependence of fracture density on elevation in either landscape (e.g., Riebe et al., 2015). We interpret the scatter in Fig. 2c to reflect some combination of variability in rock properties within a single cliff (e.g., local hydrology, cliff aspect, or fracture orientation, connectivity, and aperture), deviation from equilibrium or threshold conditions, and the limitations of the Culmann slope stability model to describe the mechanics of rock failure in these landscapes.

**Channel grain size and width measurements.** We quantified grain size and channel width using high-resolution (8-14 cm/pixel) orthophotos of channels at the interface of the mountain front and alluvial fan for each catchment (Fig. DR6). By focusing on channels at the head of alluvial fans, we ensured that the grain size distributions measured are readily mobilized and not locally derived from landslides or rockfall. Additionally, transport distances from hillslope to fan are short (<10 km) and thus we hypothesize that the coarse sediment grain size distribution in fans remains sensitive to the fracture density on bedrock hillslopes (e.g., Sklar et al., 2017). We emphasize that this approach aims to identify minimum reasonable thresholds for river incision applied to steadily eroding watersheds. We did not account for effects of local hillslope-channel coupling whereby large immobile blocks may armor the channel bed (e.g., Shobe et al., 2016).

For each channel, we used the grid-by-number method (Bunte and Abt, 2001) to measure the apparent b-axis dimension of all clasts intersecting a 2 m grid overlaid along a channel and fan area of  $10^3 \text{ m}^2$  ( $N = 175\text{-}300$  for each channel). The minimum resolved grain diameter was set to 4 pixels, and grid intersections obscured by vegetation or water were not included in the grain size distribution. We defined grain size measurements below the resolving limit (32-56 cm) as “fine” and included these values in the construction of cumulative grain size distributions. For the NSJM fans, more than 50% of the counted grains were resolvable, and thus we were able to estimate the median grain size as  $D_{50} = 58 \text{ cm}$ . For the ESGM fans, only the coarsest 25% of the grains were resolvable. Assuming similar sorting, the ratio of the 84<sup>th</sup> percentile of the grain size distribution between the NSJM ( $D_{84} = 140\text{-}175 \text{ cm}$ ) and the ESGM ( $D_{84} = 44\text{-}51 \text{ cm}$ ) is  $\sim 3$ . Alternatively, comparing the median grain size from the NSJM fans to the median grain size from field surveys throughout the San Gabriel Mountains ( $D_{50} = 9 \text{ cm}$ ; DiBiase and Whipple, 2011) results in a grain size ratio of  $\sim 6$ . Channel widths for Cucamonga Creek and Snow Creek were calculated visually, using vegetation patterns along banks to define channel boundaries, and defining average channel width as the mapped channel area divided by thalweg length (Fig. DR6).

**Stochastic-threshold incision model.** We used a bedrock river incision model (Lague et al., 2005) that combines a shear stress incision law with a threshold (Howard and Kerby, 1983) with a stochastic distribution of flood events:

$$E = \int_{Q_c}^{Q_m} I(Q, k_{sn}, k_{wn}, D_{50}) pdf(Q) dQ, \quad (4)$$

where the long-term bedrock incision rate,  $E$ , is the integrated product of the instantaneous incision law,  $I$ , and the probability distribution of discharge events,  $pdf(Q)$ , and  $Q_c$  and  $Q_m$  are the discharge magnitudes that define the limits of integration. For most of the parameter space relevant to the ESGM and NSJM field areas, Equation (4) converges quickly and is insensitive to the choice of  $Q_m$  (Lague et al., 2005). Instantaneous incision is modeled at a daily time step and itself depends on daily discharge,  $Q$ , the normalized channel steepness index,  $k_{sn} = SA^{-\theta_{ref}}$ , the channel width index,  $k_{wn} = wA^{-\omega_{ref}}$ , and the median grain diameter,  $D_{50}$ . The normalized channel steepness index encapsulates the downstream reduction in channel slope,  $S$ , with increasing drainage area,  $A$  (Wobus et al., 2006), and the channel width index similarly encapsulates downstream increases in channel width,  $w$  (Lague, 2014). We fixed the empirically-derived exponents  $\theta_{ref}$  and  $\omega_{ref}$  to be dimensionally consistent and match the observed concavity of bedrock rivers ( $\theta_{ref} = 0.45$ ;  $\omega_{ref} = 0.55$ ) (DiBiase and Whipple, 2011). The median grain diameter,  $D_{50}$ , determines the threshold overcome for incipient motion of sediment mantling the channel bed and thus provides a minimum estimate of the magnitude of the incision threshold for bedrock erosion. Although bare bedrock reaches, including waterfalls, exist in both ESGM and NSJM channels (Fig. 1d, 1e), most of the channel network is mantled by sediment. Following DiBiase and Whipple (2011), we assumed a generalized Darcy-Weisbach friction relationship and a shear stress-incision exponent equal to 1.5, such that the instantaneous incision rate can be simplified as:

$$I = K_1 \left( \frac{Q}{\bar{Q}} \right)^{0.75} \left( \frac{\bar{Q}}{A} \right) \frac{k_{sn}}{k_{wn}} - K_2 D_{50}^{1.5}, \quad (5)$$

where  $K_1$  is a constant that incorporates rock erodibility, flow resistance, and gravity,  $K_2$  is a constant that incorporates rock erodibility, density, and gravity,  $Q/\bar{Q}$  is daily discharge normalized to a reference (mean) value, and  $\bar{Q}/A$  is mean runoff. The normalized critical discharge required for incision,  $Q/\bar{Q} = Q_c/\bar{Q}$ , can be obtained by setting  $I = 0$  and rearranging Equation (5):

$$\frac{Q_c}{\bar{Q}} = K_3 \left( \frac{\bar{Q}}{A} \right)^{-4/3} \left( \frac{k_{wn}}{k_{sn}} \right)^{4/3} D_{50}^2, \quad (6)$$

where  $K_3 = (K_2/K_1)^{4/3}$  and depends only on frictional, gravity, and density effects (i.e., does not incorporate rock erodibility). Importantly, the dependence of the critical discharge on the steepness index, the width index, and grain size leads to a nonlinear dependence of long term incision rate on these parameters (Lague, 2014), in contrast to models that assume a constant effective discharge (Whipple and Tucker, 1999; Sklar and Dietrich, 2004). Based on analysis of modern daily streamflow data in the ESGM and NSJM, we defined the probability distribution of flood events using an inverse gamma distribution that combines a power-law tail for large floods with an exponential tail of low-flow events:



$$pdf(Q) = \frac{(\bar{Q}k)^{k+1}}{\Gamma(k+1)} \exp\left(-k \frac{\bar{Q}}{Q}\right) Q^{-(2+k)}, \quad (7)$$

where  $\bar{Q}$  is the mean daily discharge,  $k$  is a parameter that determines discharge variability (low  $k$  = high variability), and  $\Gamma$  is the gamma function. For a full derivation of equations (4-7), see Lague et al. (2005) and DiBiase and Whipple (2011).

We calibrated the above model according to data from the San Gabriel Mountains (Table DR1, Table DR2; DiBiase and Whipple, 2011), which include the ESGM, and we highlight in Fig. 3c the effect of increasing grain size by a factor of 3-6. Because runoff distributions are similar for Cucamonga Creek in the ESGM and Snow Creek in the NSJM (Fig. 3a, Fig. DR2, DR3), we held constant  $k = 0.5$  and mean runoff,  $\bar{Q}/A = 0.8$  mm/day. As a first comparison, we held all other parameters constant to isolate the effect of grain size, which we increased by a factor of 3-6x based on photo-derived measurements and field measurements from the San Gabriel Mountains (Fig. 3b, Fig. DR6). We estimated the channel width index for both landscapes based on orthophoto-derived measurements of channel width from the alluvial fan heads of Cucamonga Creek ( $w = 6.5$  m,  $A = 26$  km<sup>2</sup>,  $k_{wn} = 1.1$  m/km<sup>1.1</sup>) and Snow Creek ( $w = 8.7$  m,  $A = 28$  km<sup>2</sup>,  $k_{wn} = 1.4$  m/km<sup>1.1</sup>), where vegetated banks clearly define channel geometry (Fig. DR6). These preliminary measurements indicate that channels in the NSJM are slightly wider (a factor of 1-1.5x), but we note that further field work is needed to assess how channel width varies throughout each landscape, as dense riparian vegetation limits the effectiveness of remote sensing analysis. Although we lack quantitative data to evaluate the relative changes in intrinsic rock erodibility between the two landscapes, the contrast in erosional efficiency between the ESGM and NSJM implies a contrast in incision threshold that is consistent with initial motion thresholds inferred from differences in channel-bed grain size distributions.

**Headwater colluvial channel morphology.** To analyze the morphology of headwater colluvial channel networks, we first delineated colluvial and fluvial channels based on scaling breaks observed in log-log plots of channel gradient versus upstream contributing area, where longitudinal profiles of colluvial channels tend to have constant slopes and fluvial channels are concave up (Montgomery and Foufoula-Georgiou, 1993; DiBiase et al., 2012) (Fig. DR8a). For each colluvial channel segment, we recorded the mean channel profile slope using least-squares regression for the region between an upstream limit of  $A = 10^4$  m<sup>2</sup> and a downstream limit of the colluvial-fluvial scaling transition. We determined the mean colluvial channel slope,  $S_c$ , based on the length-weighted average of all colluvial channels within each catchment (Fig. DR8b).

**Catchment-averaged erosion rate calculations.** To standardize erosion rate measurements from different sources (DiBiase et al., 2010; DiBiase et al., 2012; Heimsath et al., 2012; Rossi, 2014; Table DR2), we recalculated catchment-averaged in situ <sup>10</sup>Be production rates using the CRONUS-Earth online calculator (<https://hess.ess.washington.edu/>, version 2.3; Balco et al., 2008) with an effective elevation determined from catchment hypsometry (Portenga and Bierman, 2011) and based on the constant production rate model (Lal, 1991; Stone, 2000).

**Table DR1.** Parameters used for stochastic-threshold incision model.

Parameter	ESGM value	NSJM value	units
$K_1$	$1.4 \times 10^{-7}$	$1.4 \times 10^{-7}$	$\text{m}^{-1}$
$K_2$	$4.8 \times 10^{-8}$	$4.8 \times 10^{-8}$	$\text{m}^{-0.5}\text{s}^{-1}$
$D_{50}$	9	27-54	cm
$k_{\text{sn}}$	130-180	220-280	$\text{m}^{0.9}$
$k_{\text{wn}}$	1.1	1.1-1.7	$\text{m}/\text{km}^{1.1}$
$\bar{Q}/A$	0.8	0.8	mm/day
$Q_c/A$	4-6	20-190	mm/day
$Q_m/A$	5000	5000	mm/day
$k$	0.5	0.5	dimensionless

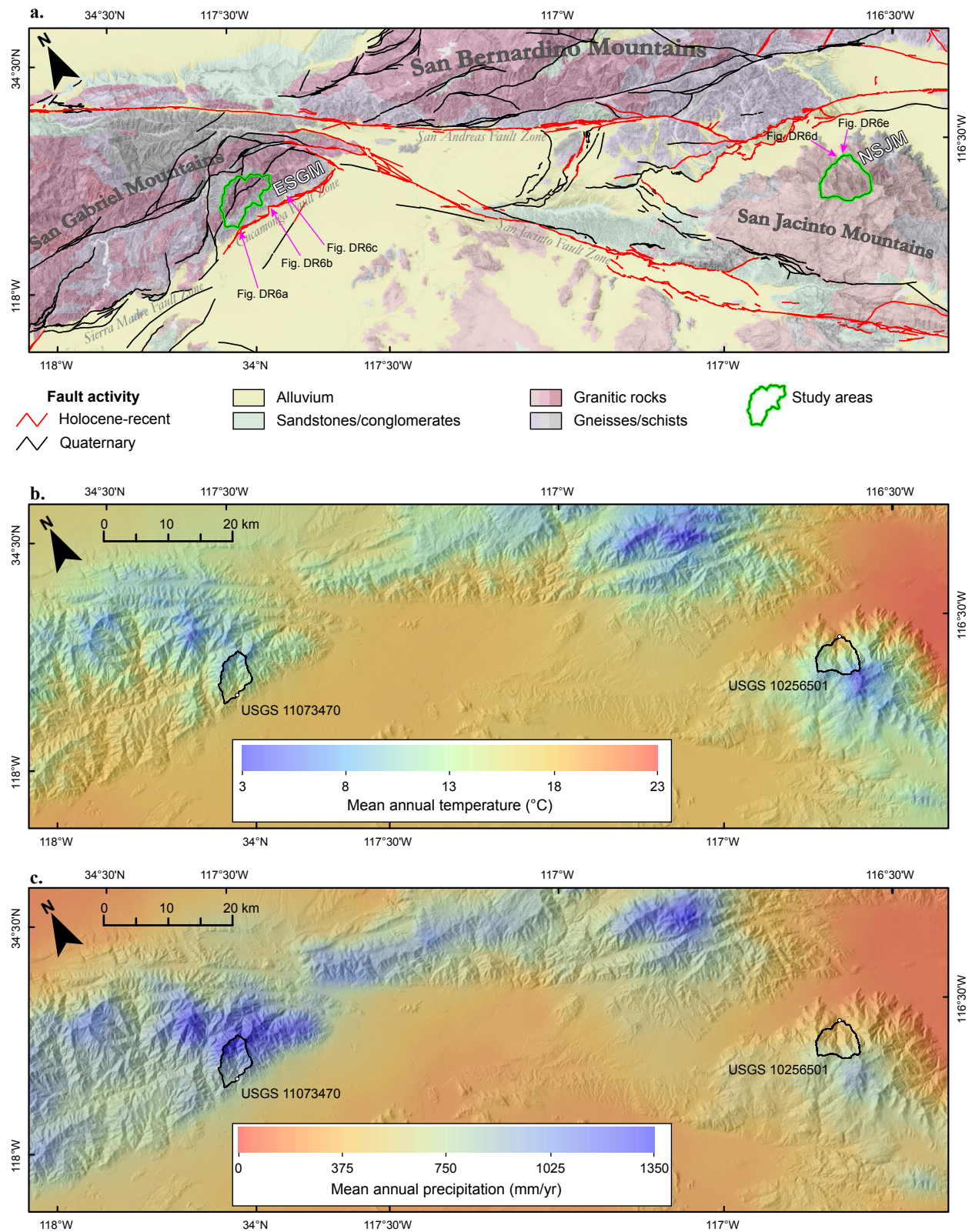


**Figure DR1.** Overview map of Eastern San Gabriel Mountains (ESGM) and Northern San Jacinto Mountains (NSJM). **a.** Geologic data from Ludington et al. (2007) and fault data from

U.S. Geological Survey and California Geological Survey (Quaternary fault and fold database for the United States, accessed December 1, 2015, from <https://earthquake.usgs.gov/hazards/qfaults/>). Arrows indicate location of alluvial fan head channels shown in Fig. DR6. **b.** Mean annual temperature (30-year normals covering 1981-2010 (<http://prism.oregonstate.edu>)). **c.** Mean annual precipitation (30-year normals covering 1981-2010 (<http://prism.oregonstate.edu>)). Location of USGS stream gages for Cucamonga Creek (USGS 11073470) in the ESGM and Snow Creek (USGS 10256500, 10256501) in the NSJM are shown in **b.** and **c.**, with black outlines indicate watershed draining to each gage.

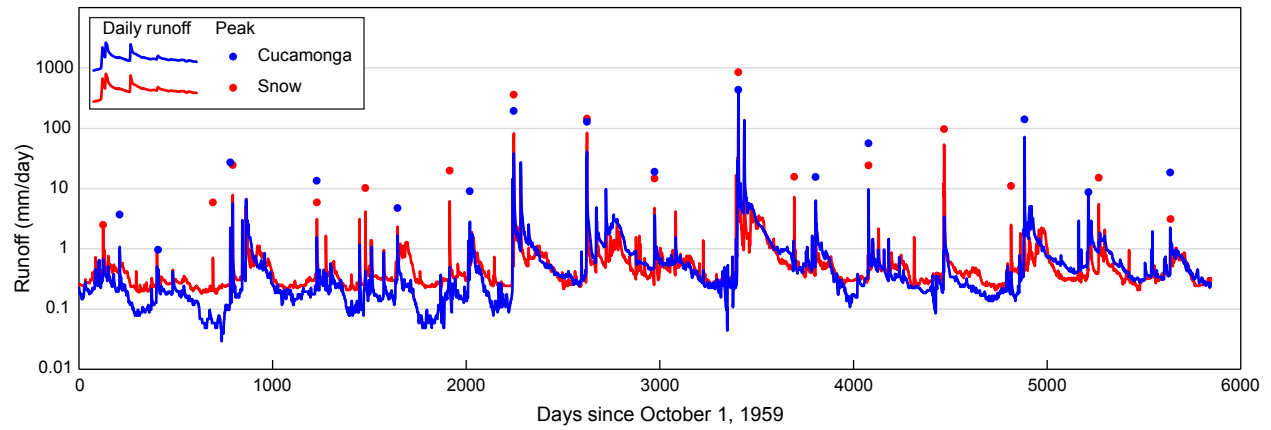


**Figure DR2.** Comparison of runoff records for Cucamonga Creek (ESGM) and Snow Creek (NSJM) during 16 year period of overlapping records beginning water year 1960. Solid lines indicate mean daily runoff (mean daily discharge divided by drainage area), and individual points indicate peak instantaneous runoff for each water year. Similar peak flow timing and magnitude suggests both watersheds likely experience common storm events.

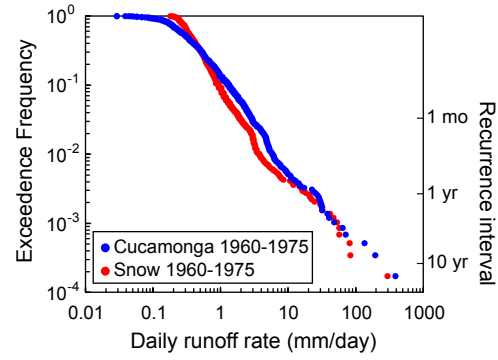


**Figure DR3.** Daily runoff records for Cucamonga Creek and Snow Creek for the overlapping period water year 1960-1975, highlighting similar frequency-magnitude relationship.

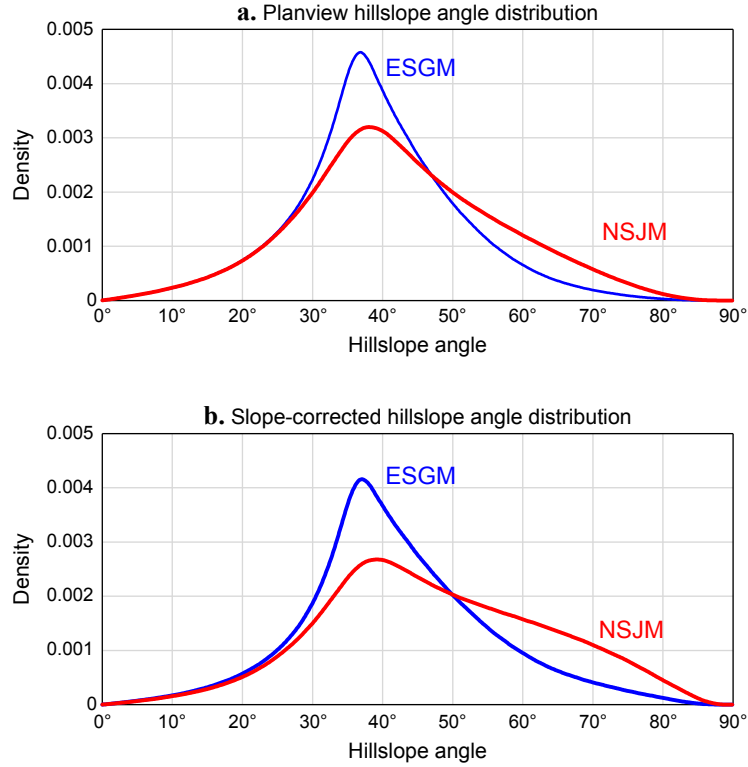


**Figure DR4.** Plan view and slope-corrected kernel density plots of hillslope angle for the Eastern San Gabriel Mountains (ESGM) and Northern San Jacinto Mountains (NSJM). **a.** Plan view hillslope angle distribution. **b.** Slope-corrected hillslope angle distribution where density has been weighted by a factor of  $1/\cos \theta$  to correct for plan view distortion (same as Fig. 1c). Note the indication of bimodal slope distribution in NSJM, which we interpret to reflect the contrast between soil-mantled hillslopes with a mode of  $\sim 38^\circ$  and bedrock hillslopes, with a mode of  $65\text{--}70^\circ$  (Fig. 2c). Bimodality is less pronounced in ESGM due to less bedrock exposed, and lower bedrock hillslope angle of  $55\text{--}60^\circ$  (Fig. 2c).



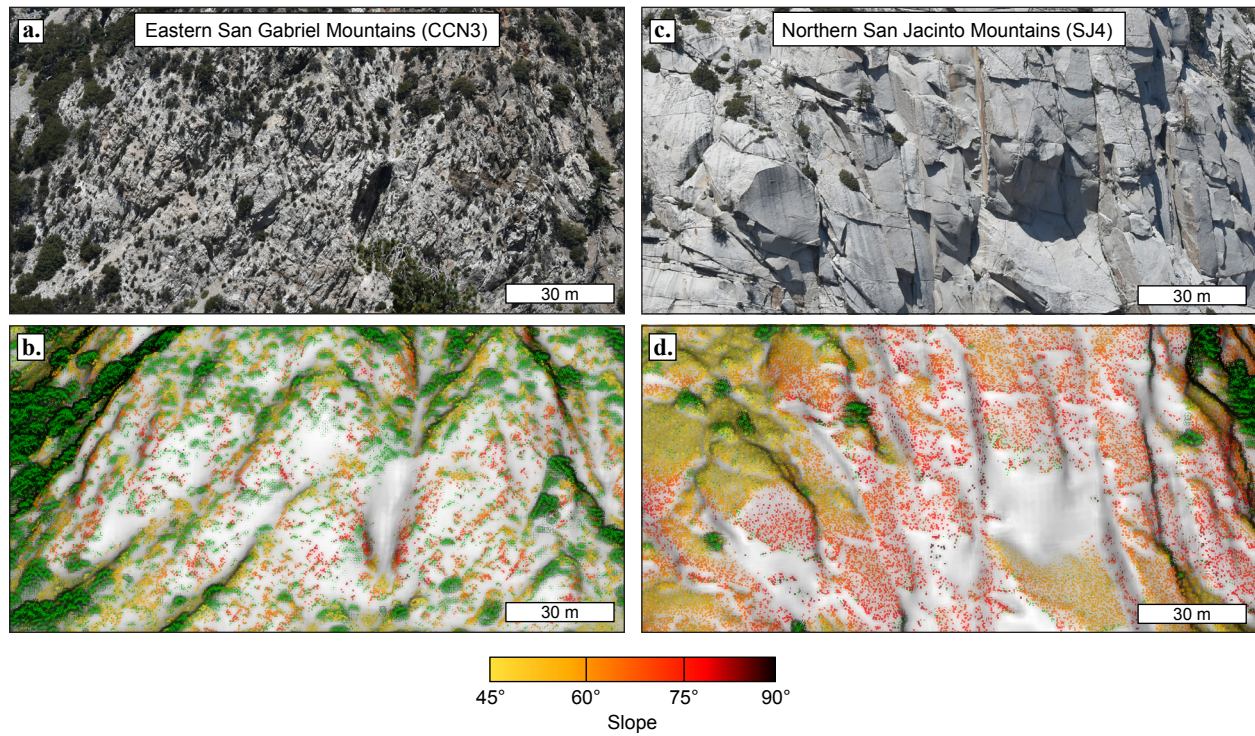


**Figure DR5.** Comparison of photographs and lidar point cloud data of bedrock cliffs shown in Fig 2a and Fig 2b. **a.** Photograph of cliff CCN3 in the Eastern San Gabriel Mountains (see Supplementary Dataset S1). **b.** Perspective view of lidar data for same extent, showing ground return points colored by point-cloud-derived slope (5 m local window), vegetation returns colored green, and interpolated mesh of bare-earth surface in grey. **c.** Photograph of middle portion of cliff SJ4 in the Northern San Jacinto Mountains (see Supplementary Dataset S1). **d.** Perspective view of lidar data for same extent, with similar symbology as **b.** Scale is similar for all panels.



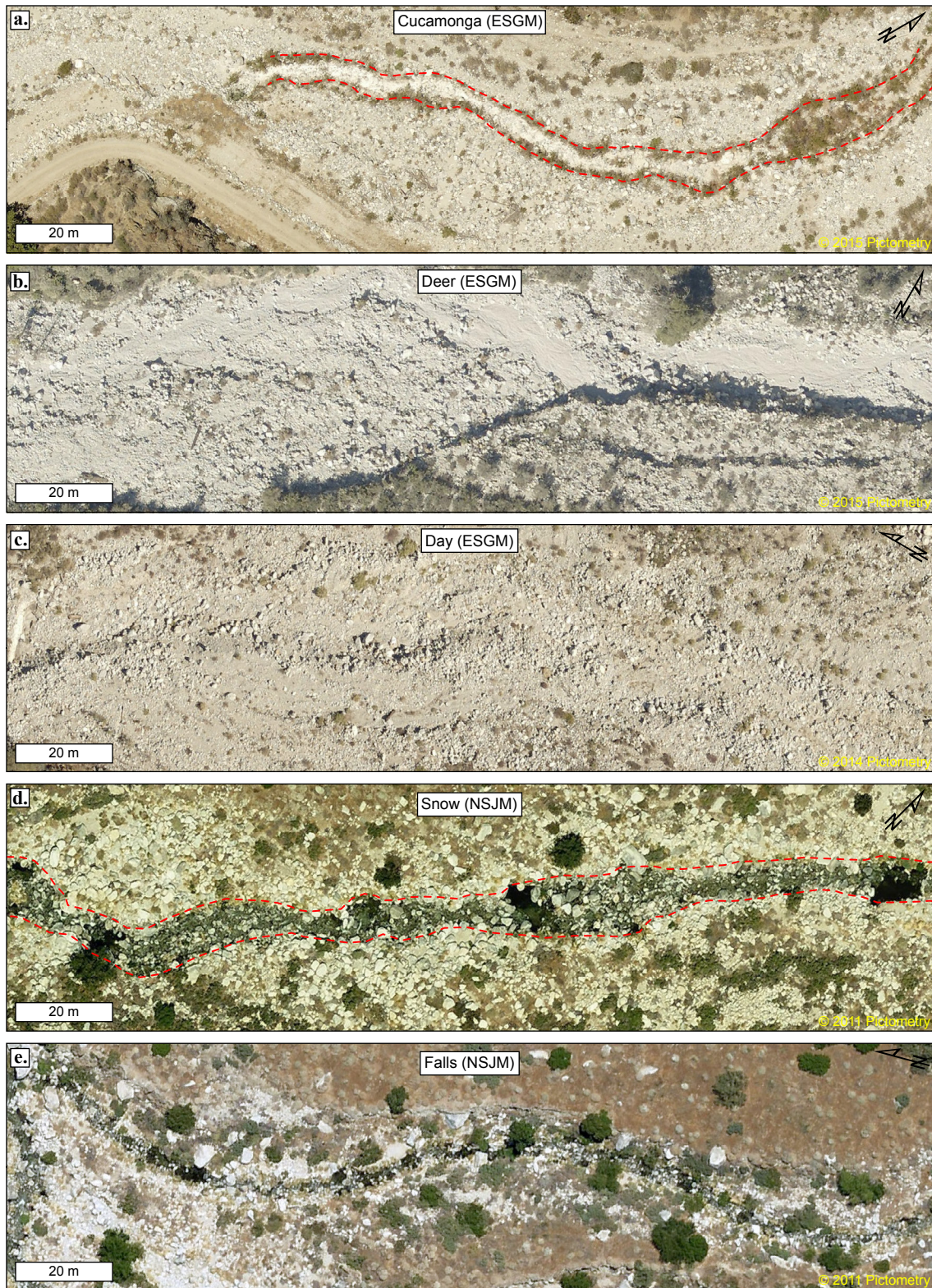


**Figure DR6.** Orthophotos of reaches used for grain size analysis on alluvial fan heads for each major drainage in the ESGM and NSJM study areas, and channel width analysis for Cucamonga Creek and Snow Creek. Dashed lines in **a.** and **d.** indicate inferred active channel boundaries used for width measurement.



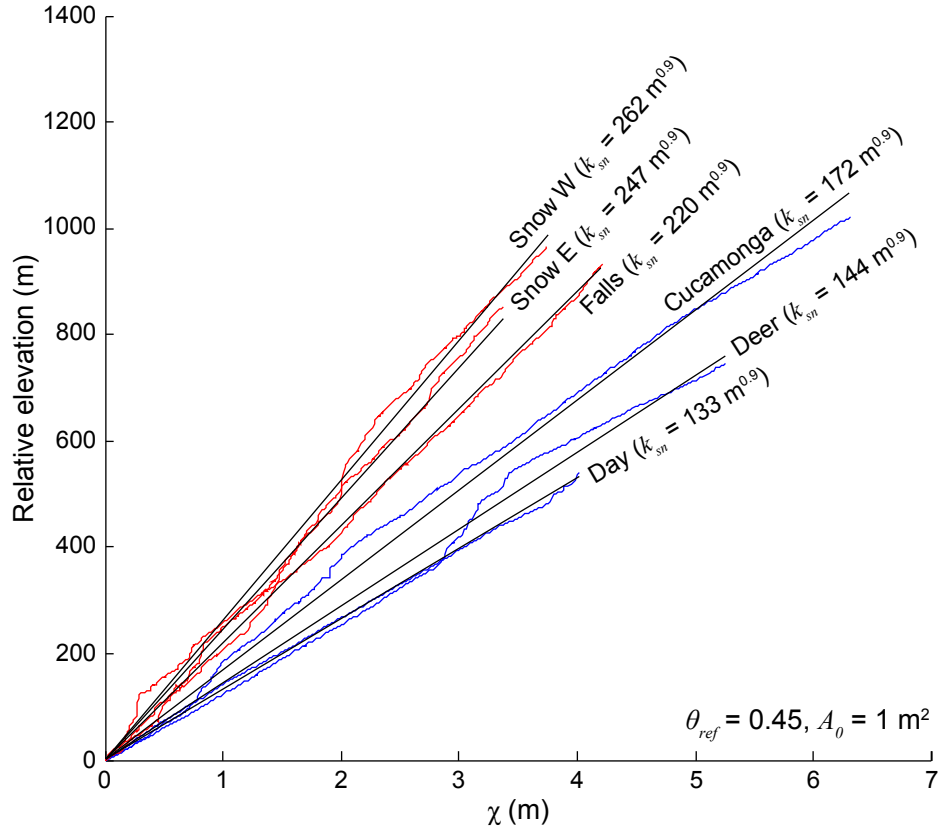


**Figure DR7.** Chi-elevation plots (Perron and Royden, 2013) of mainstem channels in the ESGM (blue) and NSJM (red), highlighting range of channel steepness index for each landscape. Reference concavity index,  $\theta_{ref}$ , is assumed to be 0.45, and reference drainage area,  $A_\theta$ , is set to  $1 \text{ m}^2$ , such that the slope of the curves is equal to the normalized channel steepness index,  $k_{sn}$  (Wobus et al., 2006).

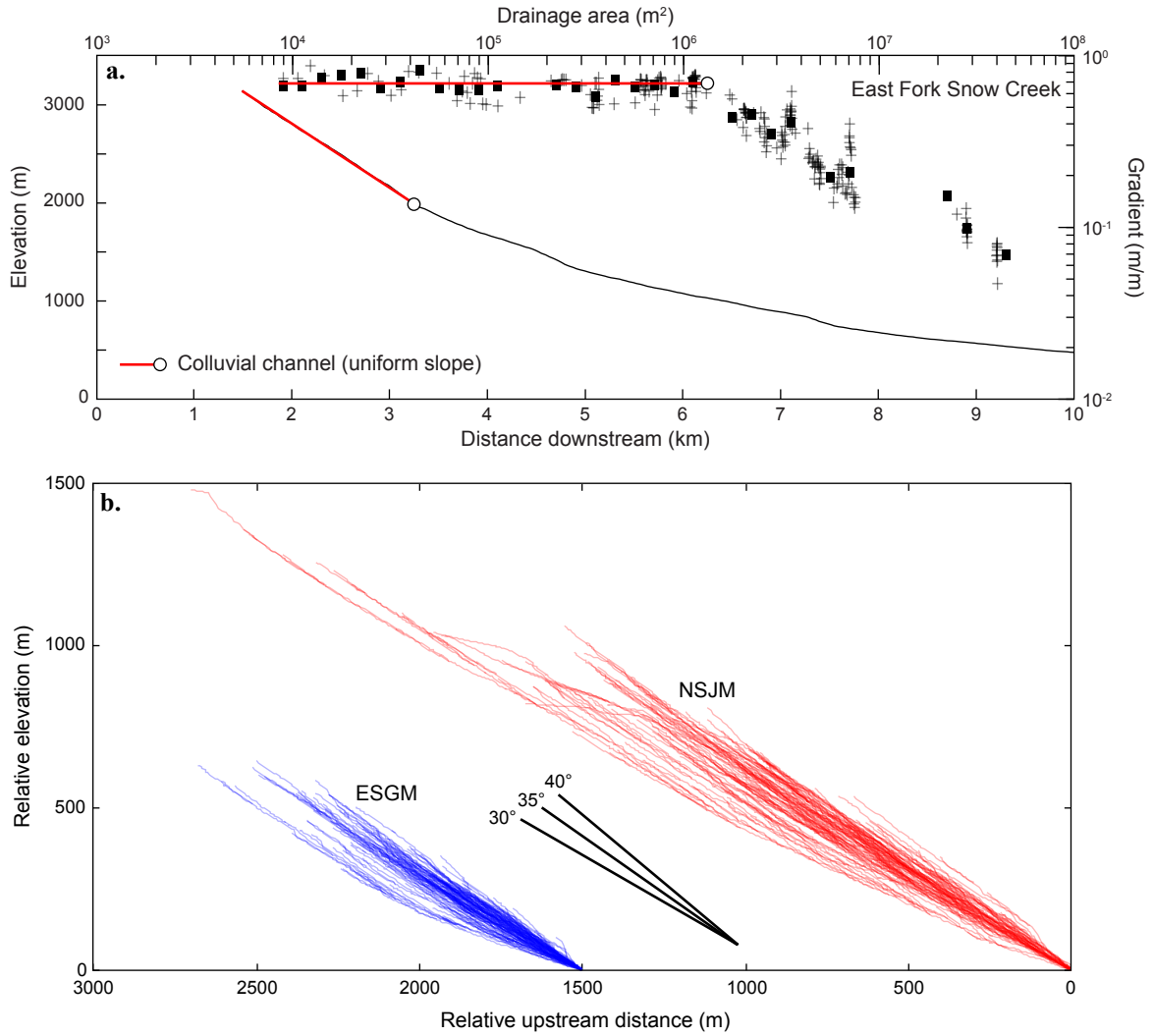


**Figure DR8.** Colluvial channel slope analysis. **a.** Slope-area plot and longitudinal profile for East Fork Snow Creek (NSJM). Crosses indicate slope and area extracted from longitudinal profile sampled at a 12 m vertical interval. Squares indicate log-binned averages. Red lines and circles indicate extent of uniformly-sloped colluvial channel. **b.** Stacked longitudinal profiles of all colluvial channels from ESGM (blue) and NSJM (red), highlighting similarity in the colluvial channel slope,  $S_c$ , between the ESGM and NSJM and greater colluvial channel relief in the NSJM. Colluvial channels for the NSJM are plotted with the colluvial-fluvial transition starting at relative distance = 0, while the ESGM colluvial channels are shifted by 1500 m for clarity. Black lines indicate slopes of  $30^\circ$ ,  $35^\circ$ , and  $40^\circ$  for reference. In both landscapes, some colluvial channels exhibit non-linear profiles that reflect slight decreases in slope typically associated with tributary junctions.



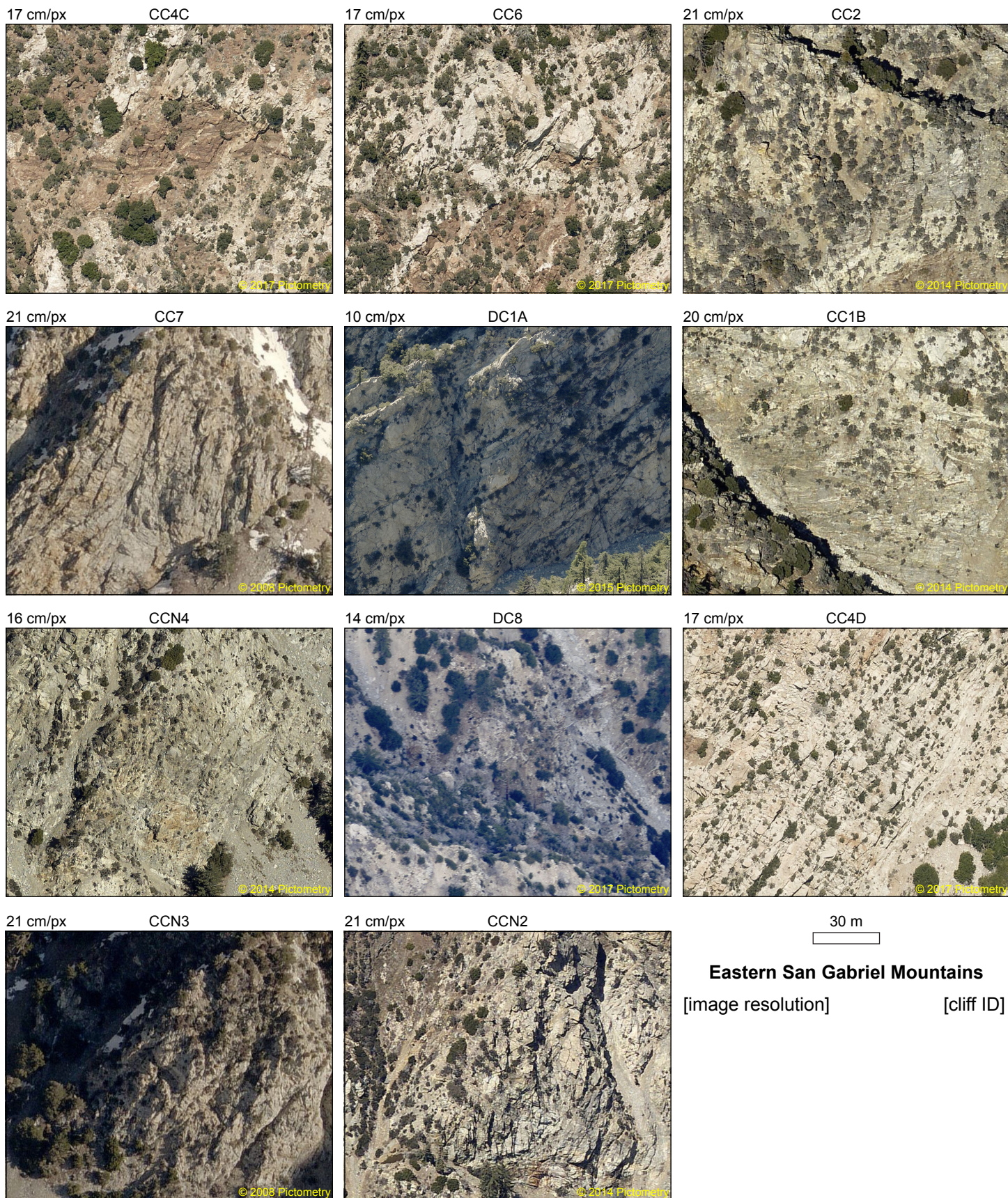


**Figure DR9.** Oblique air photographs of ESGM cliffs analyzed in Fig. 2c. All images are at similar scale. See Supplementary Dataset for locations of individual cliffs.



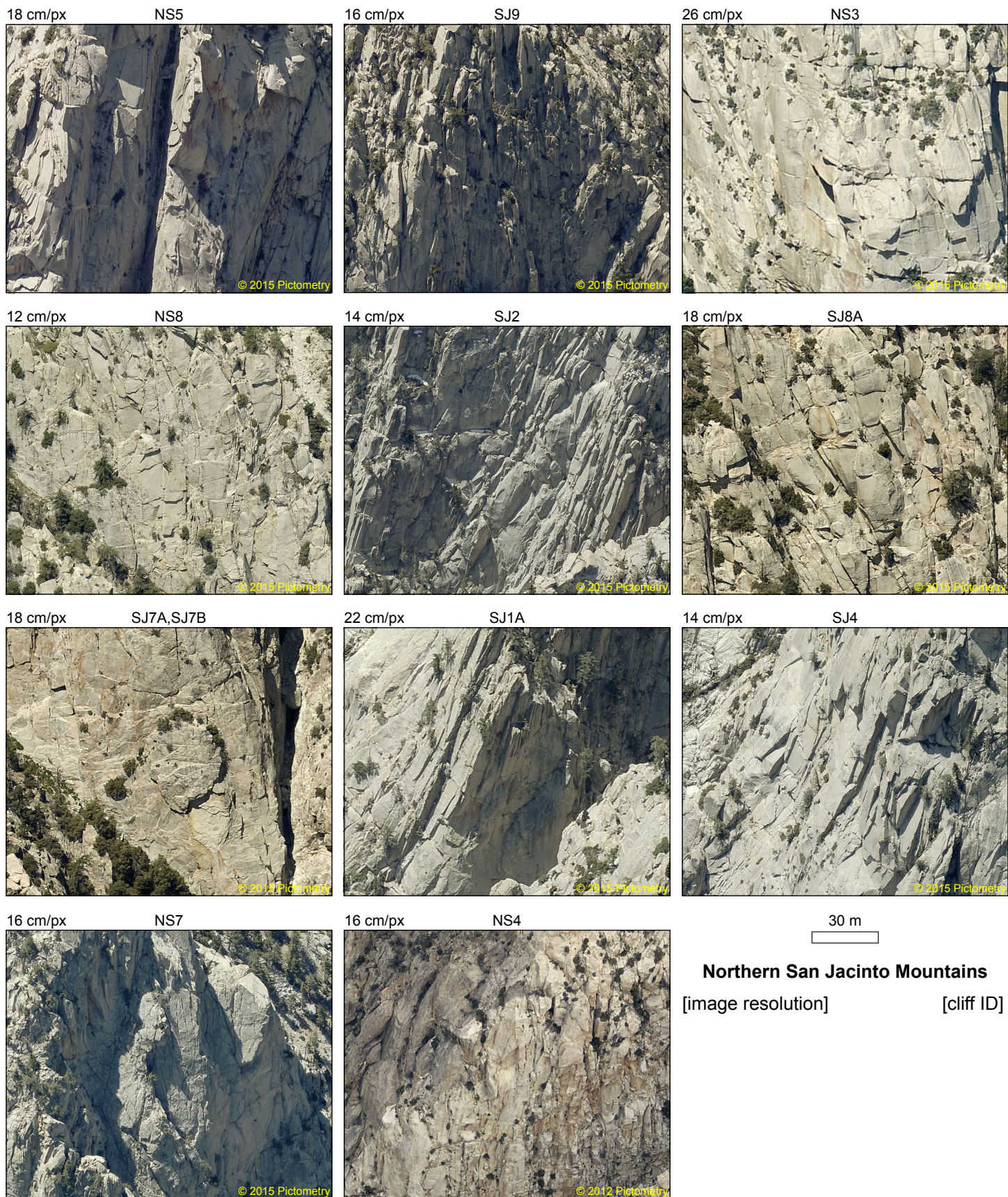


**Figure DR10.** Oblique air photographs of NSJM cliffs analyzed in Fig. 2c. All images are at similar scale. See Supplementary Dataset for locations of individual cliffs.



## References Cited

- Bunte, K., and Abt, S. R., 2001, Sampling surface and subsurface particle-size distributions in wadable gravel-and cobble-bed streams for analyses in sediment transport, hydraulics, and streambed monitoring. Gen. Tech. Rep. RMRS-GTR-74. Fort Collins, CO: U.S. Department of Agriculture, Forest Service, Rocky Mountain Research Station. 428 p.
- DiBiase, R. A., Heimsath, A. M., and Whipple, K. X., 2012, Hillslope response to tectonic forcing in threshold landscapes: *Earth Surface Processes and Landforms*, v. 37, no. 8, p. 855-865.
- DiBiase, R. A., and Whipple, K. X., 2011, The influence of erosion thresholds and runoff variability on the relationships among topography, climate, and erosion rate: *Journal of Geophysical Research*, v. 116, p. F04036.
- Heimsath, A. M., DiBiase, R. A., and Whipple, K. X., 2012, Soil production limits and the transition to bedrock-dominated landscapes: *Nature Geoscience*, v. 5, no. 3, p. 210-214.
- Howard, A. D., and Kerby, G., 1983, Channel changes in badlands: *Geological Society of America Bulletin*, v. 94, no. 6, p. 739-752.
- Lague, D., 2014, The stream power river incision model: evidence, theory and beyond: *Earth Surface Processes and Landforms*, v. 39, no. 1, p. 38-61.
- Lague, D., Hovius, N., and Davy, P., 2005, Discharge, discharge variability, and the bedrock channel profile: *Journal of Geophysical Research: Earth Surface*, v. 110, no. F4.
- Lal, D., 1991, Cosmic ray labeling of erosion surfaces: in situ nuclide production rates and erosion models: *Earth and Planetary Science Letters*, v. 104, no. 2-4, p. 424-439.
- Ludington, S., Moring, B. C., Miller, R. J., Stone, P. A., Bookstrom, A. A., Bedford, D. R., Evans, J. G., Haxel, G. A., Nutt, C. J., and Flynn, K. S., 2007, Preliminary integrated geologic map databases for the United States: Western States: California, Nevada, Arizona, Washington, Oregon, Idaho, and Utah. Version, v. 1.
- Montgomery, D. R., and Foufoula-Georgiou, E., 1993, Channel Network Source Representation Using Digital Elevation Models: *Water Resources Research*, v. 29, no. 12, p. 3925-3934.
- Perron, J. T., and Royden, L., 2013, An integral approach to bedrock river profile analysis: *Earth Surface Processes and Landforms*, v. 38, no. 6, p. 570-576.
- Portenga, E. W., and Bierman, P. R., 2011, Understanding Earth's eroding surface with  $^{10}\text{Be}$ : *GSA Today*, v. 21, no. 8, p. 4-10.
- Riebe, C. S., Sklar, L. S., Lukens, C. E., and Shuster, D. L., 2015, Climate and topography control the size and flux of sediment produced on steep mountain slopes. *Proceedings of the National Academy of Sciences*, v. 112, no. 51, p. 15574-15579.
- Rossi, M. W., 2014, Hydroclimatic Controls on Erosional Efficiency in Mountain Landscapes, PhD Thesis, Arizona State University.
- Schmidt, K. M., and Montgomery, D. R., 1995, Limits to relief: *Science*, v. 270, no. 5236, p. 617-620.
- Shobe, C. M., Tucker, G. E., and Anderson, R. S., 2016, Hillslope-derived blocks retard river incision. *Geophysical Research Letters*, v. 43 no. 10, p. 5070-5078.
- Sklar, L. S., and Dietrich, W. E., 2004, A mechanistic model for river incision into bedrock by saltating bed load: *Water Resources Research*, v. 40, no. 6.
- Sklar, L. S., Riebe, C. S., Marshall, J. A., Genetti, J., Leclerc, S., Lukens, C. L., and Mercier, V., 2017, The problem of predicting the size distribution of sediment supplied by hillslopes to rivers: *Geomorphology*, v. 277, p. 31-49.

- Stone, J. O., 2000. Air pressure and cosmogenic isotope production: *Journal of Geophysical Research: Solid Earth*, v. 105, no. B10, p. 23753-23759.
- Whipple, K. X., and Tucker, G. E., 1999, Dynamics of the stream-power river incision model: Implications for height limits of mountain ranges, landscape response timescales, and research needs: *Journal of Geophysical Research: Solid Earth*, v. 104, no. B8, p. 17661-17674.
- Wobus, C., Whipple, K.X., Kirby, E., Snyder, N., Johnson, J., Spyropolou, K., Crosby, B., and Sheehan, D., 2006, Tectonics from topography: Procedures, promise, and pitfalls. *Geological Society of America Special Papers*, 398, p.55-74.

**Table DR2. Cosmogenic nuclide erosion rate data and sources used in Figure 3C**

Sample ID	Data source	Outlet Longitude (WGS 1984)	Outlet Latitude (WGS 1984)	Catchment Area (km <sup>2</sup> )	Mean $k_{sn}$ (m <sup>0.9</sup> )	$k_{sn}$ error (m <sup>0.9</sup> )	Mean elevation (m)	<sup>10</sup> Be concentration (10 <sup>3</sup> atoms/g SiO <sub>2</sub> )	<sup>10</sup> Be error (10 <sup>3</sup> atoms/g SiO <sub>2</sub> )	Effective elevation (m)	Erosion rate (mm/yr)	Erosion rate error (mm/yr)
SG118	DiBiase et al., 2010	-118.0272	34.2782	6.0	43	1	1527	32.57	2.25	1515	0.244	0.025
SG123	DiBiase et al., 2010	-118.0496	34.3519	3.2	66	2	1731	93.68	3.95	1749	0.098	0.009
SG128	DiBiase et al., 2010	-118.0105	34.3381	2.1	29	8	1790	250.69	20.68	1801	0.037	0.004
SG129	DiBiase et al., 2010	-118.0122	34.3404	0.1	29	4	1788	213.83	57.3	1799	0.044	0.013
SG130	DiBiase et al., 2010	-117.9914	34.3805	0.3	27	3	1734	138.47	9.04	1741	0.065	0.007
SG131	DiBiase et al., 2010	-117.9931	34.3659	2.3	29	3	1738	102.88	12.7	1745	0.089	0.013
SG132	DiBiase et al., 2010	-117.9904	34.3657	1.1	35	4	1728	94.48	4.54	1734	0.096	0.009
SG137	DiBiase et al., 2010	-117.8900	34.2723	46.8	154	3	1524	15.05	1.4	1553	0.543	0.066
SG138	DiBiase et al., 2010	-117.8919	34.2717	17.9	131	3	1383	18.65	2.75	1398	0.396	0.067
SG140	DiBiase et al., 2010	-117.9504	34.2427	7.7	93	6	1071	32.49	1.99	1038	0.179	0.017
SG141	DiBiase et al., 2010	-117.9741	34.2539	43.1	126	4	1526	30.45	2.38	1551	0.267	0.029
SG151	DiBiase et al., 2010	-117.8002	34.3204	3.5	146	17	2290	34.82	10.27	2328	0.380	0.127
SG157	DiBiase et al., 2010	-117.7313	34.3056	25.4	173	5	2019	11.68	1.57	2100	0.988	0.156
SG158	DiBiase et al., 2010	-117.7332	34.3058	53.2	145	3	1949	11.68	1.39	2010	0.935	0.134
SG159	DiBiase et al., 2010	-117.7416	34.2959	35.0	178	4	1958	17.15	1.67	2029	0.644	0.081
SG161	DiBiase et al., 2010	-117.7623	34.3027	11.6	164	7	1954	12.03	1.69	2009	0.907	0.148
SG162	DiBiase et al., 2010	-117.6362	34.1649	28.0	172	6	1570	33.69	4.63	1638	0.255	0.041
SG163	DiBiase et al., 2010	-117.6362	34.1650	28.0	172	6	1570	43.13	2.83	1638	0.199	0.020
SG206	DiBiase et al., 2010	-117.7922	34.2320	5.4	81	12	862	18.56	5.21	816	0.273	0.086
SG207	DiBiase et al., 2010	-117.8065	34.2408	6.5	89	3	1053	23.04	2.33	1031	0.252	0.032
SGB1	DiBiase et al., 2010	-118.1573	34.3060	174.7	62	6	1401	73.21	14.6	1393	0.107	0.024
SGB2	DiBiase et al., 2010	-118.1086	34.3062	102.0	63	6	1448	69.03	17.25	1431	0.116	0.032
SGB3	DiBiase et al., 2010	-118.1219	34.3113	106.9	63	6	1437	96.74	13.99	1443	0.083	0.014
SGB5	DiBiase et al., 2010	-118.1210	34.3301	9.9	60	1	1358	56.53	10.86	1338	0.134	0.029
SGB6	DiBiase et al., 2010	-118.2504	34.3284	9.7	115	4	1286	29.39	12.46	1258	0.246	0.129
SGB7	DiBiase et al., 2010	-118.1488	34.2980	3.2	106	8	1311	29.16	4.74	1286	0.253	0.046
SGB9	DiBiase et al., 2010	-118.2560	34.3029	17.3	118	3	1139	15.33	0.56	1113	0.445	0.037
SGB10	DiBiase et al., 2010	-118.1967	34.2819	7.5	105	5	1107	22.56	0.76	1071	0.293	0.024
SGB11	DiBiase et al., 2010	-117.7403	34.2966	82.5	157	3	1953	14.82	0.67	2022	0.821	0.074
SGB12	DiBiase et al., 2010	-117.7621	34.2420	148.4	163	2	1803	11.07	0.63	1886	1.010	0.097
SGB13	DiBiase et al., 2010	-117.7425	34.2967	35.0	178	4	1959	28.22	1.84	2029	0.432	0.044
SG0703	DiBiase et al., 2010	-118.1027	34.3090	9.9	66	3	1349	12.54	0.83	1318	0.561	0.056
SG0728	DiBiase et al., 2010	-117.9011	34.3619	9.1	95	15	2088	110.91	6.08	2125	0.105	0.010
SG0729	DiBiase et al., 2010	-117.9051	34.3598	5.3	94	24	2127	155.05	7.65	2165	0.076	0.007



SG0730	DiBiase et al., 2010	-118.1636	34.3064	5.7	131	13	1174	11.55	2.64	950	0.481	0.121
SG0743	DiBiase et al., 2010	-117.9819	34.3043	22.0	113	5	1725	42.7	2.89	1759	0.217	0.022
SG160	DiBiase et al., 2012	-117.7621	34.3034	18.8	187	7	2096	14.82	2.44	2160	0.808	0.151
SG0706	DiBiase et al., 2012	-118.1027	34.1880	17.3	122	5	1138	10.79	1.91	1122	0.574	0.113
SG0747	DiBiase et al., 2012	-118.0207	34.2133	7.3	125	9	1130	11.81	3.51	1093	0.515	0.172
SG0748	DiBiase et al., 2012	-118.0199	34.2116	7.4	132	10	1125	11.77	2.61	1089	0.515	0.126
SG0749	DiBiase et al., 2012	-118.0211	34.2005	6.1	113	2	1127	10.53	2.83	1103	0.581	0.174
SG0818	DiBiase et al., 2012	-118.1764	34.2515	25.5	92	3	1255	9.98	1.33	1236	0.669	0.103
SG0803	Heimsath et al., 2012	-117.8365	34.3720	11.4	117	5	2126	46.34	5.21	2174	0.260	0.036
SG0804	Heimsath et al., 2012	-117.8368	34.3697	8.1	125	5	2175	28.51	5.01	2224	0.436	0.086
SG0805	Heimsath et al., 2012	-117.8391	34.3693	3.1	100	6	2025	36.66	4.39	2063	0.307	0.044
SG0809	Heimsath et al., 2012	-117.8255	34.3857	18.5	110	4	2062	29.97	2.61	2111	0.387	0.046
SJC0806	Rossi, 2014	-116.6803	33.8739	28.2	282	12	1859	63.68	1.67	1948	0.162	0.013
SJC0807	Rossi, 2014	-116.6737	33.8726	11.1	238	20	1776	103.55	4.91	1876	0.095	0.009